Phase field model for fracture analysis of functionally graded power-based shell structures

T. Guillén-Hernández[a], J. Reinoso[*b], M. Paggi[a]

[a] IMT School for Advanced Studies Lucca, Piazza San Francesco, 55100 Lucca, Italy

[b] Elasticity and Strength of Materials Group, School of Engineering, Universidad de Sevilla, Camino de los Descubrimientos s/n, 41092, Seville, Spain

[*] Corresponding Author: jreinoso@us.es

Phase field model for fracture analysis of functionally graded power-based shell structures

Abstract

The phase field (PF) approach of fracture has emerged as a potential modelling tool that regularizes the variational fracture theory in the spirit of Griffith's vision via the introduction of a damage-like field within the formulation. In this work, we outline a PF formulation for triggering brittle fracture phenomena in Functionally Graded Materials (FGMs) shell structures. This model relies on the 6-parameter shell formulation complying with a solid shell kinematic description and incorporates the use of the Enhanced Assumed Strain (EAS) and Assumed Natural Strain (ANS) methods in order to alleviate locking pathologies. The corresponding multi-field variational formalisms is consistently derived and discretized within the context of the Finite Element Method (FEM). Details regarding the implementation in the general purpose FE packages are outlined. The applicability of this model is demonstrated by means of several numerical applications.

Keywords: Phase Field approach to fracture; Functionally Graded Materials; Shells; EAS; ANS; Phase field length

1   Introduction

Functionally Graded Materials (FGMs) emerged in the last quarter of the last century as a suitable alternative for their application in different engineering areas. These composite materials are composed of several phases where the volume fractions of their constituents vary smoothly and continuously within the specimen domain, especially along the thickness direction. Commonly, FGMs are made of ceramic and metallic phase [1], but alternative combinations can be found in the related literature, see [2, 3] and the references given therein.

Due to the combination of different materials and also to the smooth variation of them, FGMs have very important advantages with respect to conventional materials. For example, in interfaces between conventional layer-based materials, the existing elastic mismatch on the material properties generally leads to notable interfacial stresses that can provoke the corresponding structural failure. However, using FGMs this problem is solved because the discontinuity on the material properties is highly reduced. Moreover, FGMs present good mechanical and thermal properties because they can be tailored differently depending on their applications.

As a consequence of the previous capacities, FGMs are used in a wide range of high tech applications such as bio-medics [4, 5], thermal barrier coatings [6] or sensors [7] among many others. In this regard, one of the most prominent forms for the practical use of FGMs is their incorporation as thin-walled structures which have been concurrently exploited in many engineering applications such as energy absorbing components [8, 9], structural components in aeronautics [10, 11, 12] or photovoltaic panels [13].

With the aim of the achievement the reliable characterization of different structural concepts, in the related literature, research activities on structural theories, encompassing beams, plates and shells, have attracted the attention of numerous researchers. In this setting, with special focus on shell-based structures, an impressive range of models for shells have been proposed so far. A possible categorization of the existing shell models can differentiate between classical and novel/advanced shell formulations. Thus, well-established models, known as Classical Shell Theories (CST), recall the popular Kirchhoff-Love (3-parameter) and Reissner-Mindlin (5-parameter) theories [14, 15]. Both of such CST make some mechanical assumptions across the thickness advocating the *dimensional reduction* concept that allows referring the magnitudes to the shell midsurface. However, Kirchhoff-Love (3-parameter) and Reissner-Mindlin (5-parameter) theories inherently imply the adoption of relevant hypotheses regarding the out-of-plane response of the shell body, which directly embody the simplification of the constitutive

tensor via a plane stress formulation. Note that in both CST formulations additionally render the assumption concerning of the inextensibility the shell director vector which means that, the strains in the thickness direction are not taken into consideration. To overcome this limitation, Higher Order Theories (HOT) have been developed in the last two decades. Within this context, Carrera proposed the so-called Unified Formulation (CUF) [16]. In brief, the CUF is an axiomatic model that is postulated via the consistent expansion of the displacement field (u_i) complying with the following scheme:

$$u_i = u_{0i} + z^j u_{ji} \qquad with \quad i = x, y, z \quad and \quad j = 1, ..., N \qquad (1)$$

being N the order of expansion and u_{0i} the displacement of the mid-reference surface in the i direction. This formulation is able to cover the equivalent single layer (ESL) and the Layer-wise (LW) approaches [17, 18] in an amenable and robust manner.

Alternative to CUF-based models, continuum-based shell elements have been extensively exploited in the last years, with especial attention to the so-called solid shell kinematic model and the corresponding finite element discretization schemes, see [19, 20, 21] and the references therein given. Despite the appealing aspect of such solid shell formulations, including the avoidance of rotations and the fully 3D description of the shell body, their corresponding discrete models using low-oder (namely first-order) displacements interpolation are prone to suffer from locking. These locking pathologies provide artificially stiffer solutions, and their circumventions are usually performed using numerical techniques such as the Enhanced Assumed Strain method (EAS), the Assumed Natural Strain method (ANS) and the Reduced Integration formulations [22, 23, 24, 25, 26, 27]. Specialized previous shell models for FGMs, the reader is referred to fundamental references, see [28, 29, 30, 31, 32].

Furthermore, the technical importance of shells in many industrial sectors motivates the development of predictive modelling methods for the accurate prediction of fracture events in such components. Nonetheless, this is a very challenging task due to the imbrication of curved geometries, potential geometrical nonlinear effects, among other aspects. In this concern, different fracture formulations have been formulated in the related literature during the last years such as the Extended-FEM (X-FEM) [33, 34], cohesive zone models (CZM) [35, 36, 37, 38, 39] to quote a few of them. Particularly, both X-FEM and CZ techniques fall into the category of *strong discontinuous crack methods*, which present notable difficulties in tracking the crack path and require the adoption of ad-hoc criteria for crack initiation and propagation criteria.

In contrast to the previous cracking methodologies, *smeared crack* techniques can be conceived as potential modelilng tools for triggering fracture phenomena in solids. Specifically, the so-called phase field (PF) approach of fracture is characterized by the introduction of a damage-like field within the formulation, regularizing the variational formalism associated with the fracture theory of Griffith. PF methods permit the simulation of complex fracture phenomena in very elegant and consistent manner with the only use of physically sound material parameters [40, 41, 42, 43]. Further investigations on PF methods for triggering fracture recall the development of parametric insensitive approaches for brittle and quasi-brittle materials [44, 45], anisotropic PF models for composite materials [46], hydrogen-assisted cracking events [47], the corresponding coupling of PF and interface crack methods for heterogeneous media [48, 49, 50], ductile fracture [51], and FGMs [52], among many others.

Despite the notable development of PF in the last years, the application of such numerical methodology for shells has received a limited attention. Similarly to PF for solids, the variational formalism for cracking shells encompasses the contribution to the total energy functional of the elastic and the fracture counterparts. In this concern, Amiri et al. [53] derived a PF model for thin shells via the adoption of the KirchoffLove (3-parameter) kinematics via the local maximum entropy mesh-free method, whereas alternative PF formulations for shells can

be found in [54, 53]. However, to the best authors' knowledge, the PF shell models aforementioned are not locking-free. In order to remedy this aspect, Reinoso et al. [19] proposed a new modelling framework for solid shell model equipped with PF capabilities, which endowed the combined use of the EAS and the ANS for locking issues, and exhibited very promising results and robustness for large and small strain applications [55, 50].

Stemming from the previous arguments, in this work, we propose a new formulation to simulate fracture of functionally graded (FG) power-based shells. In the current model here proposed, the phase field model of brittle fracture is employed in combination with the 6-parameter adopting a solid shell kinematic description as baseline structural model. Moreover, as recalled above, the present model integrates two methods to alleviate locking pathologies: the Enhanced Assumed Strain (EAS) method and the Assumed Natural Strain (ANS) method [30], rendering a locking-free finite element formulation. Finally, the proposed approach also accounts for the spatial variation along the thickness direction of the elastic and fracture properties as well as the phase field length scale [52].

The paper is arranged as follows. In Section 2 the basis of the phase field model are presented. The 6-parameter shell formulation is given in Section 3. In Section 4, the spatial variation of FGMs material properties is addressed. In Section 5 there are different numerical examples showing some applications of the model presented in this paper. Finally, in Section 6, the main conclusions of this investigation are exposed.

2   Phase Field approach of brittle fracture

This section presents the basis aspects of the phase field (PF) approach for brittle fracture [43], whose application to FGMs does not imply any substantial modification of the fundamental formalism. Note also that the following formulation is restricted to Kirchhoff-Saint-Venant material models, being the corresponding extension to nonlinear material formulations beyond the scope of the present research [19, 55].

As point of departure, let us consider an arbitrary shell body whose reference placement is identified by $\mathcal{B}_0$ ($\mathcal{B}_0 \subset \mathbb{R}^3$). This shell body experiences a motion $\boldsymbol{\varphi}(\mathbf{X}, t)$: $\mathcal{B}_0 \times [0, t] \longrightarrow \mathbb{R}^3$, where $[0, t]$ is the time step interval that maps the reference material points ($\mathbf{X} \in \mathcal{B}_0$) onto the current material points ($\mathbf{x} \in \mathcal{B}_t$). Therefore, the transformation between the reference and the current coordinates can be expressed as: $\mathbf{x} = \boldsymbol{\varphi}(\mathbf{X}, t)$, see Fig.1.
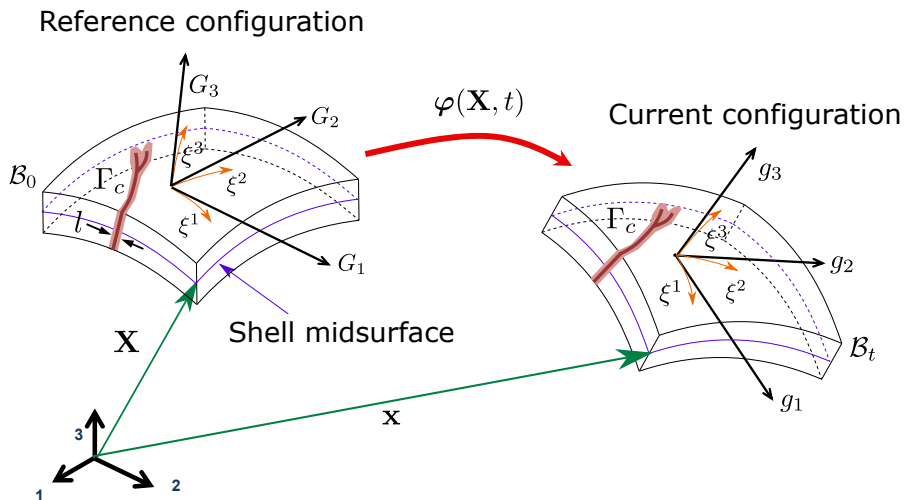

Figure 1: Description of an arbitrary cracking shell body. Distinction between the reference and current placements.
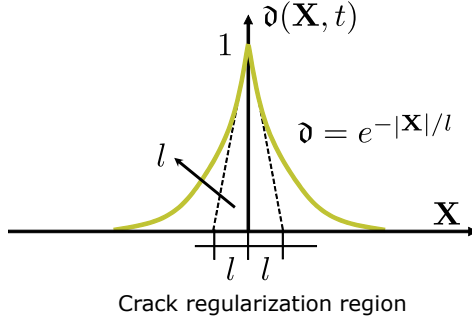
Figure 2: Diffusive crack modelling solution for the one dimensional crack problem.

It can be noticed in Fig.1 the presence of a diffusive crack, which complies with the main hypothesis of the PF methods of fracture, i.e. a discrete crack is regularized within a diffusive crack zone of width l. Fig.2 depicts a simple regularization scheme in 1D based on the length scale parameter l which rules the width of the regularization region and retrieving a sharp crack representation as l tends to zero.

This regularization is characterized through the introduction of the scalar-valued function $\mathfrak{d}$, which is called the phase field or damage parameter. This phase field variable is assumed to be a smooth function with the body domain $\mathfrak{d}(\mathbf{X}, t)$, identifying intact and fully damage states for $\mathfrak{d} = 0$ and $\mathfrak{d} = 1$, respectively.

One fundamental ingredient for the exploitation of PF methods is the introduction of the crack surface density functional $\gamma(\mathfrak{d}, \nabla_{\mathbf{X}}\mathfrak{d})$ which allows the following approximation of the fracture energy due to the crack formation:

$$\int_{\Gamma_c} \mathcal{G}_c \, \mathrm{d}\partial\Omega \approx \int_{\mathcal{B}_0} \mathcal{G}_c \gamma(\mathfrak{d}, \nabla_{\mathbf{X}}\mathfrak{d}) \, \mathrm{d}\Omega, \tag{2}$$

where $\mathcal{G}_c$ is the fracture toughness, with:

$$\gamma(\mathfrak{d}, \nabla_{\mathbf{X}}\mathfrak{d}) = \frac{1}{2l}\mathfrak{d}^2 + \frac{l}{2}\left|\nabla_{\mathbf{X}}\mathfrak{d}\right|^2, \tag{3}$$

being $\nabla_{\mathbf{x}}\mathfrak{d}$ the spatial gradient of $\mathfrak{d}(\mathbf{X}, t)$.

The resemblance of the PF method of continuum damage mechanics (CDM)-based models is advocated by the affection of the phase field damage variable on the elastic free energy of the body. This is conducted by means of the definition of degradation function $\mathfrak{g}(\mathfrak{d}) = [1 - \mathfrak{d}]^2$, so that the elastic free energy of the body can be rewritten as: $\psi(\boldsymbol{\varepsilon}, \mathfrak{d}) = \mathfrak{g}(\mathfrak{d})\psi^e(\boldsymbol{\varepsilon})$, where $\psi^e(\boldsymbol{\varepsilon})$ is the intact elastic free energy.

Accordingly, the internal part of the potential energy functional that defines the current coupled deformation-fracture problem (See Fig.1) can be expressed as the sum of the elastic energy stored in the shell body and the energy necessary to create new crack fronts:

$$\Pi_{int}(\mathbf{u}, \mathfrak{d}) = \int_{\mathcal{B}_0} \psi(\varepsilon, \mathfrak{d}) \, \mathrm{d}\Omega + \int_{\mathcal{B}_0} \mathcal{G}_c(\mathbf{X})\gamma(\mathfrak{d}, \nabla_{\mathbf{x}}\mathfrak{d}) \, \mathrm{d}\Omega = \Pi_{el}(\boldsymbol{\varepsilon}, \mathfrak{d}) + \Pi_{frac}(\mathbf{X}, \mathfrak{d}, \nabla_{\mathbf{x}}\mathfrak{d}) \tag{4}$$

Note that in the previous expression, we explicitly introduced the spatially varying fracture toughness $\mathcal{G}_c(\mathbf{X})$ for its application to FGMs.

The strain energy density of the body is constructed via the exploitation of the spectral decomposition with the aim of splitting the positive and negative contributions [48, 43]. Recalling the spatially varying material properties, where the material properties are expressed in terms of

the material coordinates $\mathbf{X}$, the corresponding free energy function for Kirchhoff-Saint-Venant material models is given by:

$$\psi(\boldsymbol{\varepsilon}, \mathfrak{d}, \mathbf{X}) = \mathfrak{g}(\mathfrak{d})\psi_+^e(\boldsymbol{\varepsilon}, \mathbf{X}) + \psi_-^e(\boldsymbol{\varepsilon}), \tag{5a}$$

$$\psi_+^e(\boldsymbol{\varepsilon}, \mathbf{X}) = \frac{\lambda(\mathbf{X})}{2}\left(\langle \mathrm{tr}[\boldsymbol{\varepsilon}]\rangle_+\right)^2 + \mu(\mathbf{X})\mathrm{tr}[\boldsymbol{\varepsilon}_+^2], \tag{5b}$$

$$\psi_-^e(\boldsymbol{\varepsilon}, \mathbf{X}) = \frac{\lambda(\mathbf{X})}{2}\left(\langle \mathrm{tr}[\boldsymbol{\varepsilon}]\rangle_-\right)^2 + \mu(\mathbf{X})\mathrm{tr}[\boldsymbol{\varepsilon}_-^2], \tag{5c}$$

where $\lambda(\mathbf{X})$ y $\mu(\mathbf{X})$ are the Lamé constants that depend on the material coordinates for FGMs; $\boldsymbol{\varepsilon}_+$ and $\boldsymbol{\varepsilon}_-$ respectively stand for the positive and negative parts of the infinitesimal strain tensor, whilst the symbol $\mathrm{tr}[\bullet]$ identifies the trace operator and $\langle \bullet \rangle_\pm$ denotes the Macaulay bracket: $\langle \bullet \rangle_\pm = (\bullet \pm |\bullet|)/2$.

In line with [41, 42], it is worth mentioning that the internal length scale of the PF method, l, can be associated with the apparent strength of the material according to the following expression:

$$l = \frac{27E\mathcal{G}_C}{256\sigma_c^2} \tag{6}$$

being $\mathcal{G}_C$ the fracture toughness, E the young modulus and σ_c the nominal strength of the material.

The particularization of the previous expression for FGMs requires the consideration of the variation of the material properties within the domain, i.e. $\mathcal{G}_C(\mathbf{X})$, $E(\mathbf{X})$ and $\sigma_c(\mathbf{X})$ leading to $l(\mathbf{X})$ (contrasting with the approach proposed in [52]). In the particular case of FGM-shells, this spatial variation of the elastic and the material properties will be considered as a function of the thickness coordinate of the shell body ξ^3 without any loss of generality.

Finally, the irreversibility of the evolution of the phase field crack variable character of the crack evolution is ensured through the consideration of a local history variable [43]:

$$\mathcal{H}(\mathbf{X}, t) = \max_{\tau \in [0,t]} \psi_+^e(\boldsymbol{\varepsilon})(\mathbf{X}, t), \tag{7}$$

where $\mathcal{H}$ is the maximal value of the positive part of the elastic energy $\psi_+^e(\boldsymbol{\varepsilon})$, that is identified as the crack driving force.

3 The locking free solid shell 7-parameter shell model

In this section, the main aspects of the current 7-parameter solid shells model for the simulation of shell structures are summarized [19, 21]. In particular, Sect. 3.1 outlines the kinematics of the solid shell model that defines the basic 6-parameter formulation, whereas the use of the EAS and ANS methods is detailed in Sects. 3.2 and 3.3. Finally, the variational formalism combining the current solid shell model and the PF method is recalled in Sect. 3.4.

3.1 Solid shell kinematic formulation: 6-parameter shell model

In line with the basic notation introduced in the previous section, let to consider an arbitrary shell body which experiences a motion $\boldsymbol{\varphi}(\mathbf{X}, t)\colon \mathcal{B}_0 \times [0, t] \longrightarrow \mathbb{R}^3$, such that $\mathbf{x} = \boldsymbol{\varphi}(\mathbf{X}, t)$, see Fig.1.

The position vectors at the reference ($\mathbf{X}$) and current ($\mathbf{x}$) configurations are functions of the parametric curvilinear coordinates $\boldsymbol{\xi} = \{\xi^1, \xi^2, \xi^3\}$, where $\xi^i \in [-1, 1]$ with $i = [1, 2, 3]$. Note that as customary in shell models, the coordinates $\{\xi^1, \xi^2\}$ identify the in-plane shell

coordinates, whereas ξ^3 stands for the thickness shell coordinate. The position vector of any point in the reference configuration can be interpolated by the position vectors of the top $\mathbf{X}_t$ and bottom $\mathbf{X}_b$ surfaces:

$$\mathbf{X}\{\xi^1, \xi^2, \xi^3\} = \frac{1}{2}[1 + \xi^3]\mathbf{X}_t(\xi^1, \xi^2) + \frac{1}{2}[1 - \xi^3]\mathbf{X}_b(\xi^1, \xi^2) \tag{8}$$

Rearranging the previous expression, one finds:

$$\mathbf{X}\{\xi^1, \xi^2, \xi^3\} = \frac{1}{2}[\mathbf{X}_t(\xi^1, \xi^2) + \mathbf{X}_b(\xi^1, \xi^2)] + \frac{1}{2}\xi^3[\mathbf{X}_t(\xi^1, \xi^2) - \mathbf{X}_b(\xi^1, \xi^2)] = \mathbf{R}(\xi^1, \xi^2) + \xi^3\mathbf{A}_3(\xi^1, \xi^2), \tag{9}$$

where $\mathbf{R}(\xi^1, \xi^2)$ is the shell midsurface position vector and $\mathbf{A}_3(\xi^1, \xi^2)$ is the shell director vector, both defined in the reference configuration.

Following the same procedure with the position vector in the current configuration, the result is very similar as can be seen in the expression:

$$\mathbf{x}\{\xi^1, \xi^2, \xi^3\} = \frac{1}{2}[\mathbf{x}_t(\xi^1, \xi^2) + \mathbf{x}_b(\xi^1, \xi^2)] + \frac{1}{2}\xi^3[\mathbf{x}_t(\xi^1, \xi^2) - \mathbf{x}_b(\xi^1, \xi^2)] = \mathbf{r}(\xi^1, \xi^2) + \xi^3\mathbf{a}_3(\xi^1, \xi^2) \tag{10}$$

where $\mathbf{r}(\xi^1, \xi^2)$ is the position vector of the shell midsurface and $\mathbf{a}_3(\xi^1, \xi^2)$ is the shell director vector, both in the current configuration; $\mathbf{x}_t(\xi^1, \xi^2)$ and $\mathbf{x}_b(\xi^1, \xi^2)$ stand for the position vectors of the top and bottom surfaces in the current configuration, respectively.

Therefore, the displacement field is given by

$$\mathbf{u}(\boldsymbol{\xi}) = \mathbf{x}(\boldsymbol{\xi}) - \mathbf{X}(\boldsymbol{\xi}) = \mathbf{v}(\xi^1, \xi^2) + \xi^3\mathbf{w}(\xi^1, \xi^2) \tag{11}$$

where $\mathbf{v}(\xi^1, \xi^2)$ and $\mathbf{w}(\xi^1, \xi^2)$ are the displacement vectors of the shell midsurface and the director vector:

$$\mathbf{v}(\xi^1, \xi^2) = \frac{1}{2}[\mathbf{u}_t(\xi^1, \xi^2) + \mathbf{u}_b(\xi^1, \xi^2)] \tag{12}$$

$$\mathbf{w}(\xi^1, \xi^2) = \frac{1}{2}[\mathbf{u}_t(\xi^1, \xi^2) - \mathbf{u}_b(\xi^1, \xi^2)]. \tag{13}$$

In the previous expressions, $\mathbf{u}_t(\xi^1, \xi^2)$ and $\mathbf{u}_b(\xi^1, \xi^2)$ denote the displacement vectors of the top and bottom surfaces, respectively.

The covariant basis vectors in the reference $(\mathbf{G}_i(\boldsymbol{\xi}))$ and current $(\mathbf{g}_i(\boldsymbol{\xi}))$ configurations are:

$$\mathbf{G}_i(\boldsymbol{\xi}) = \frac{\partial\mathbf{X}(\boldsymbol{\xi})}{\partial\xi^i}; \qquad \mathbf{g}_i(\boldsymbol{\xi}) = \frac{\partial\mathbf{x}(\boldsymbol{\xi})}{\partial\xi^i} = \mathbf{G}_i(\boldsymbol{\xi}) + \frac{\partial\mathbf{u}(\boldsymbol{\xi})}{\partial\xi^i}; \qquad i = 1, 2, 3; \tag{14}$$

and satisfy the standard relations: $G_i.G^j = \delta_i{}^j$ and $g_i.g^j = \delta_i{}^j$, being $\delta_i{}^j$ the Kronecker delta. Then, the metric coefficients are: $G_{ij} = G_iG_j$ and $g_{ij} = g_ig_j$.

Finally, the Jacobi matrices to do the transformations between the parametric space in the reference $\mathbf{J}(\boldsymbol{\xi})$ and in the current configurations $\mathbf{j}(\boldsymbol{\xi})$), are defined by:

$$\mathbf{J}(\boldsymbol{\xi}) = [\mathbf{G}_1(\boldsymbol{\xi}), \mathbf{G}_2(\boldsymbol{\xi}), \mathbf{G}_3(\boldsymbol{\xi})]^{\mathrm{T}}; \qquad \mathbf{j}(\boldsymbol{\xi}) = [\mathbf{g}_1(\boldsymbol{\xi}), \mathbf{g}_2(\boldsymbol{\xi}), \mathbf{g}_3(\boldsymbol{\xi})]^{\mathrm{T}} \tag{15}$$

The displacement derived deformation gradient, $\mathbf{F}^u$, and the displacement derived Green-Lagrange deformation tensor, $\mathbf{E}^u$, take the forms:

$$\mathbf{F}^u := \mathbf{g}_i \otimes \mathbf{G}^i, \tag{16}$$

$$\mathbf{E}^u := \frac{1}{2}\left[(\mathbf{F}^u)^{\mathrm{T}}\mathbf{F}^u - \mathbb{I}_2\right] = \frac{1}{2}\left[g_{ij} - G_{ij}\right]\mathbf{G}^i \otimes \mathbf{G}^j, \tag{17}$$

where $\mathbb{I}_2$ stands for the second-order identity tensor in the curvilinear setting. Finally, the second Piola-Kirchhoff stress tensor is given by:

$$\mathbf{S} = S^{ij}\mathbf{G}_i \otimes \mathbf{G}_j, \tag{18}$$

where S^{ij} identify the corresponding contravariant components.

3.2 The EAS method: 7-parameter shell model

In this Section, the principal concepts regarding the EAS method are presented. Note that the application of this numerical methodology to the previous 6-parameter solid shell formulation leads to the so-called 7-parameter shell model. Specifically, the objective of this method in the current solid shell model is the alleviation of volumetric and Poisson thickness locking effects.

The variational form of the EAS recalls the invocation of the Hu-Washizu variational principle in a Lagrangian formulation and we decompose the Green-Lagrange strain tensor ($\mathbf{E}$) into a compatible part ($\mathbf{E}^u$), which are the strains derived from the displacement, and an incompatible part ($\tilde{\mathbf{E}}$), which are called enhanced strains: $\mathbf{E} = \mathbf{E}^u + \tilde{\mathbf{E}}$.

The original form of the Hu-Washizu principle for the application of the EAS method considers 3 independent fields as primary variables, i.e. the displacement field ($\mathbf{u}$), the incompatible strain tensor ($\tilde{\mathbf{E}}$), the second Piola-Kirchhoff stress tensor ($\mathbf{S}$). However, the imposition of the orthogonality condition between the incompatible strain and the stress fields allows restricting the primary unknowns to the displacement and incompatible strain fields [23].

Accordingly, the variation of the internal potential of the shell body (precluding the role of crack evolution) adopts the form:

$$\delta\hat{\Pi}(\mathbf{u}, \delta\mathbf{u}, \tilde{\mathbf{E}}, \delta\tilde{\mathbf{E}}) = \int_{\mathcal{B}_0} \mathbf{S} : \delta\mathbf{E}^u d\Omega - \int_{\mathcal{B}_0} \mathbf{S} : \delta\tilde{\mathbf{E}} d\Omega, \quad \forall\delta\mathbf{u} \in \mathfrak{V}^u, \forall\delta\tilde{\mathbf{E}} \in \mathfrak{V}^{\tilde{E}} \tag{19}$$

where $\mathfrak{V}^u = \{\delta\mathbf{u} \in [H^1(\mathcal{B}_0)] : \delta\mathbf{u} = \mathbf{0} \text{ on } \partial\mathcal{B}_{0,u}\}$ is the space of admissible displacement variations, and $\mathfrak{V}^{\tilde{E}} = [L_2(\mathcal{B}_0)]$ denotes for the admissible space corresponding to the incompatible strains.

Complying with standard Galerkin procedures within the context of FEM [19], the interpolation of the displacement field ($\mathbf{u}$), its variation ($\delta\mathbf{u}$) and its increment ($\Delta\mathbf{u}$) can be expressed as:

$$\mathbf{u} \approx \mathbf{N}(\boldsymbol{\xi})\mathbf{d}, \ \ \delta\mathbf{u} \approx \mathbf{N}(\boldsymbol{\xi})\delta\mathbf{d}, \ \ \Delta\mathbf{u} \approx \mathbf{N}(\boldsymbol{\xi})\Delta\mathbf{d}, \tag{20}$$

where $\mathbf{N}(\boldsymbol{\xi})$ is the matrix collecting the shape functions and $\mathbf{d}$ is the nodal displacement vector at the element level.

Moreover, the interpolation of the incompatible strains at the element level is conducted using the matrix $\mathbf{M}(\boldsymbol{\xi})$, whose definition can be designed in order to address the desired locking pathologies:

$$\tilde{\mathbf{E}} \approx \mathbf{M}(\boldsymbol{\xi})\boldsymbol{\varsigma}, \ \ \delta\tilde{\mathbf{E}} \approx \mathbf{M}(\boldsymbol{\xi})\delta\boldsymbol{\varsigma}, \ \ \Delta\tilde{\mathbf{E}} \approx \mathbf{M}(\boldsymbol{\xi})\Delta\boldsymbol{\varsigma}. \tag{21}$$

where $\boldsymbol{\varsigma}$, is the vector of the discretized incompatible strains. Note that $\mathbf{M}(\boldsymbol{\xi})$, which is denominated as enhancing interpolation matrix, is expressed in the global setting. For that reason, it is necessary a transformation mapping between the parametric ($\tilde{\mathbf{M}}(\boldsymbol{\xi})$) and the global spaces ($\mathbf{M}(\boldsymbol{\xi})$), see [19]. Finally, the form of the operator $\tilde{\mathbf{M}}(\boldsymbol{\xi})$ in this work is defined as follows

[24, 21]:

$$\tilde{M}_{\xi} = \begin{bmatrix} \xi^1 & 0 & 0 & 0 & 0 & 0 & 0 \\ 0 & \xi^2 & 0 & 0 & 0 & 0 & 0 \\ 0 & 0 & \xi^3 & \xi^1\xi^3 & \xi^2\xi^3 & 0 & 0 \\ 0 & 0 & 0 & 0 & 0 & \xi^1 & \xi^2 \\ 0 & 0 & 0 & 0 & 0 & 0 & 0 \\ 0 & 0 & 0 & 0 & 0 & 0 & 0 \end{bmatrix} \tag{22}$$

After the insertion of the discretized operators into the corresponding residual forms, the current formulation preserves the computational efficiency of standard shell models, setting the displacement degrees of freedom as the exclusive nodal unknowns via static condensation procedures.

3.3 The ANS method

The ANS is a sort of collocation method which is combined with the previous EAS method in order to obtain a locking-free shell model. In particular, the ANS is herewith recalled for the circumvention of transverse shear and trapezoidal locking issues. To do so, the interpolation of the transverse shear (E_{13}, E_{23}) and normal (E_{33}) strain components are evaluated at some collocation points, which are given in Fig. 3.
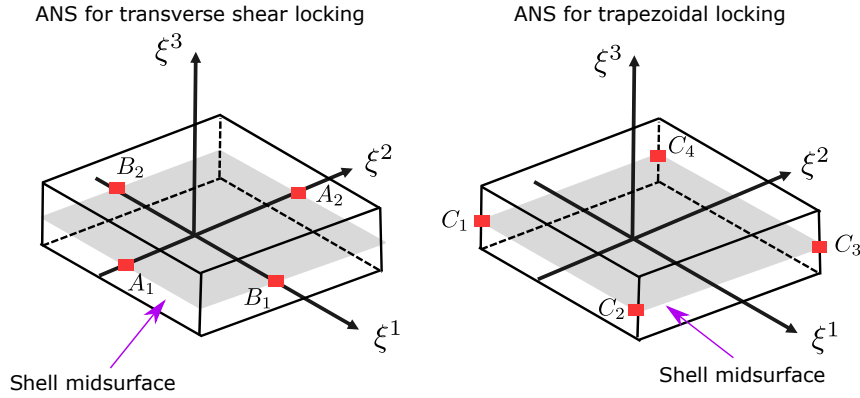

Figure 3: ANS method: definition of the collocation points in the element parametric space.

Therefore, the assumed interpolation of the transverse shear and normal strain components can be computed as:

$$E_{13}^{ANS} = \sum_{n=1}^{2} (1 + \xi_{A_i}^2 \xi^2) E_{13}(\xi_A) \tag{23a}$$

$$E_{23}^{ANS} = \sum_{n=1}^{2} (1 + \xi_{B_i}^1 \xi^1) E_{23}(\xi_B) \tag{23b}$$

$$E_{33}^{ANS} = \sum_{n=1}^{4} (1 + \xi_{C_i}^1 \xi^1)(1 + \xi_{C_i}^2 \xi^2) E_{33}(\xi_C) \tag{23c}$$

9

3.4 The phase field (PF) model of brittle fracture for locking-free shells

This Section succinctly describes the formulation of the PF model for shell fracture combined with locking-free element capabilities [50]. In a similar way to the parametrization of the material points of the shell, a linear interpolation between the top ($\mathfrak{d}_t$) and bottom ($\mathfrak{d}_b$) surfaces of the phase field damage variable is here conceived:

$$\mathfrak{d}(\xi^1, \xi^2, \xi^3) = \frac{1}{2}\left(1 + \xi^3\right)\mathfrak{d}_t(\xi^1, \xi^2) + \frac{1}{2}\left(1 - \xi^3\right)\mathfrak{d}_b(\xi^1, \xi^2),$$
$$\boldsymbol{\xi} = \left\{\xi^1, \xi^2, \xi^3\right\} \in: \square = [-1, 1] \times [-1, 1] \times [-1, 1].$$
(24)

Note that as discussed in [19], this approximation of the phase field variable permits the differentiation of the top and bottom damage states within the shell body.

The incorporation of the phase field variable as primary unknown of the coupled mechanical-crack problem can be performed via the use of the following multi-field variational formalism:

$$\Pi(\mathbf{u}, \tilde{\mathbf{E}}, \mathbf{S}, \mathfrak{d}) = \underbrace{\int_{\mathcal{B}_0 \setminus \Gamma} \mathfrak{g}(\mathfrak{d})\psi(\mathbf{E})\,\mathrm{d}\Omega - \int_{\mathcal{B}_0} \mathbf{S} : \tilde{\mathbf{E}}\,\mathrm{d}\Omega}_{\Pi_{\text{int}}} + \underbrace{\int_{\Gamma} \mathcal{G}_c(\mathbf{X})\,\mathrm{d}\Gamma}_{\Pi_{\text{fr}}} + \Pi_{\text{ext}},$$
(25)

where $\mathbf{u}$, $\tilde{\mathbf{E}}$, $\mathbf{S}$ and $\mathfrak{d}$ identify the independent fields of the formulation.

Through the adoption of the orthogonality condition between the interpolation spaces of $\tilde{\mathbf{E}}$ and $\mathbf{S}$, the variation of the previous functional with respect to the corresponding independent fields permits the construction of the work form of the initial boundary value problem (IBVP):

$$\delta\Pi^u(\mathbf{u}, \delta\mathbf{u}, \tilde{\mathbf{E}}, \mathfrak{d}) = = \int_{\mathcal{B}_0} \mathfrak{g}(\mathfrak{d})\frac{\partial\Psi}{\partial\mathbf{E}} : \delta\mathbf{E}^u\,\mathrm{d}\Omega + \delta\Pi_{\text{ext}}(\mathbf{u}) = 0, \ \ \forall\delta\mathbf{u} \in \mathfrak{V}^u$$
(26)

$$\delta\Pi^{\tilde{E}}(\mathbf{u}, \tilde{\mathbf{E}}, \delta\tilde{\mathbf{E}}, \mathfrak{d}) = \int_{\mathcal{B}_0} \mathfrak{g}(\mathfrak{d})\frac{\partial\Psi}{\partial\mathbf{E}} : \delta\tilde{\mathbf{E}}\,\mathrm{d}\Omega - \int_{\mathcal{B}_0} \mathbf{S} : \delta\tilde{\mathbf{E}}\,\mathrm{d}\Omega = 0, \ \ \forall\delta\tilde{\mathbf{E}} \in \mathfrak{V}^{\tilde{E}}$$
(27)

$$\delta\Pi^{\mathfrak{d}}(\mathbf{u}, \tilde{\mathbf{E}}, \mathfrak{d}, \delta\mathfrak{d}) = \int_{\mathcal{B}_0} -2(1 - \mathfrak{d})\delta\mathfrak{d}\Psi(\mathbf{E})\,\mathrm{d}\Omega + \int_{\mathcal{B}_0} \mathcal{G}_c(\mathbf{X})l\left[\frac{1}{l^2}\mathfrak{d}\delta\mathfrak{d} + \nabla_{\mathbf{X}}\mathfrak{d}\cdot\nabla_{\mathbf{X}}(\delta\mathfrak{d})\right]\mathrm{d}\Omega = 0,$$
$$\delta\mathfrak{d} \in \mathfrak{V}^{\mathfrak{d}},$$
(28)

where $\mathfrak{V}^{\mathfrak{d}} = \{\delta\mathfrak{d} \in \mathcal{H}^1(\mathcal{B}_0)\,|\,\delta\mathfrak{d} = 0 \text{ on } \Gamma_c\}$ denotes the space of admissible test functions for the crack phase field variable.

It is worth mentioning that the previous weak forms lead to a fully coupled system of equations that is solved using a staggered scheme between complying with a Jacobi-type formulation [43]. Finally, specific details concerning the linearization and the subsequent discretization procedures are omitted here for the sake of brevity, see [19].

4 Material formulation: power-based functionally graded materials

This Section outlines the material formulation for FGMs obeying a Kirchhoff-Saint-Venant material law with a relationship $\mathbf{S} = \mathbb{C} : \mathbf{E}$. In this concern, as stayed above, FGMs are characterized by the smooth and continuous variation of the volume fractions of the composing

constituents. For the special focus on shell-based structures, this smooth variation is herein considered normally along the thickness direction. Thus, advocating the rule of mixtures, the spatial variation of the material properties can be expressed as follows [56]:

$$p(\xi^3) = p_m f_m + p_c f_c \qquad (29)$$

where the subscripts m and c identify the two composing phases (within the scope of the present investigation the correspond to metallic and ceramic constituents), f is the volume fraction of the corresponding phase and p is a generic material property. The volume fractions are represented by the following functions:

$$f_c = \left[\frac{\xi^3}{H} + \frac{1}{2} \right]^n \qquad (30)$$

$$f_m = 1 - f_c \qquad (31)$$

where n is the volume fraction exponent ($n \geq 0$) and H is the initial thickness of the shell. Therefore, when $n = 0$ a fully ceramic material is represented. However, when n approaches infinity, a fully metallic structure is retrieved.

Through the use of the previous expression regarding the spatial variation of the material properties, it is noticing that they are dependent on the volume fraction, i.e. in the present case on the thickness coordinate ξ^3. This rule of mixture affects to: the phase field length scale (l), the Young modulus (E) and the fracture energy ($\mathcal{G}_c$) as we can see in Figures 4, 5 and 6 respectively. Note that the variation of l with respect to ξ^3 implies a novel aspect with respect to alternative PF formulations for FGMs [52].
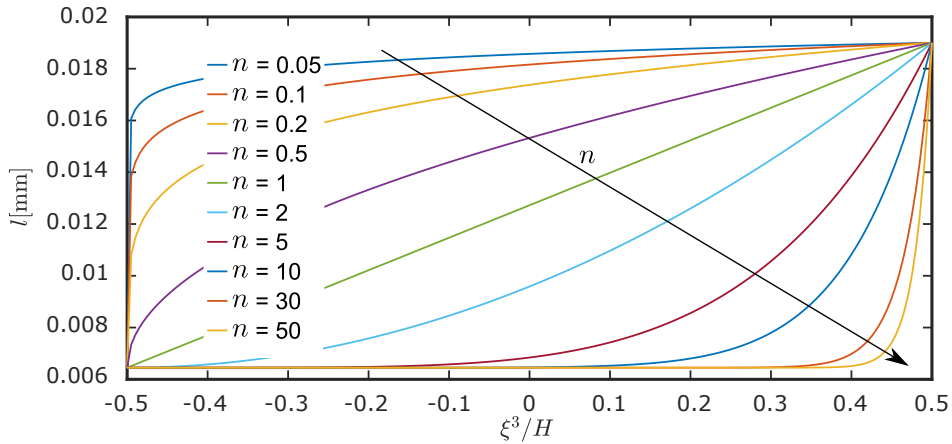

Figure 4: Variation of the phase field length (l) through the thickness (ξ^3) for different values of the volume fraction exponent (n).

5 Applications

In the present Section, several numerical examples are solved in order to demonstrate the simulation capabilities of the proposed model. In Section 5.1 a functionally graded power-based square shell under in-plane loads is simulated. However, in Sections 5.2 and 5.3, a functionally graded power-based cylindrical shell is solved under in-plane and out-of-plane loading conditions, respectively. All the examples are made of metallic and ceramic phases, and whose corresponding properties are listed in Table 1 [56, 42]. Moreover, the influence of the volume fraction exponent (n) on the applications response is analysed. Also, a comparison
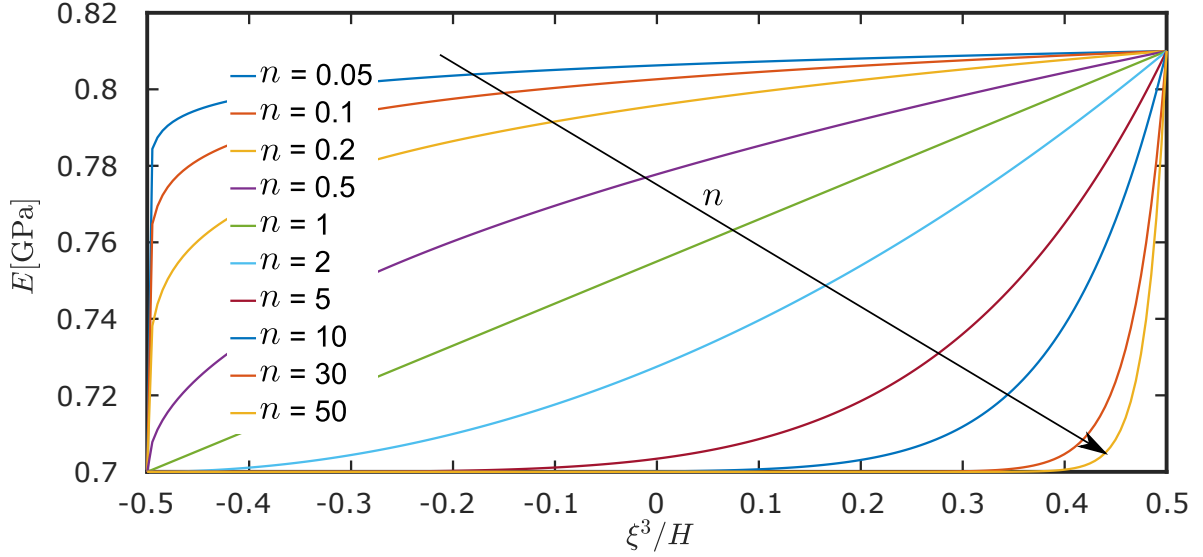
Figure 5: Variation of the young modulus (E) through the thickness (ξ^3) for different values of the volume fraction exponent (n).
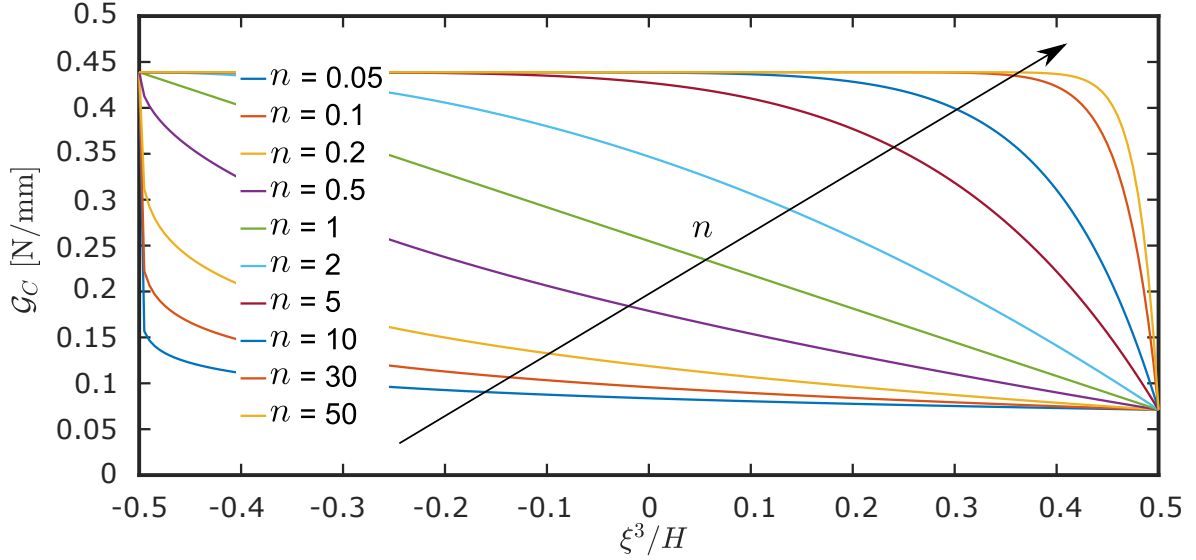

Figure 6: Variation of the critical fracture energy ($\mathcal{G}_C$) through the thickness (ξ^3) for different values of the volume fraction exponent (n).

between the results obtained with the implementation proposed in this paper and the solutions for the homogeneous solid shell formulation [19] (fully ceramic and fully metallic materials) is presented for verification purposes. Finally, it is worth mentioning that all the simulations are solved with the finite element program FEAP [57] and conducted under displacement control.

Material	E [GPa]	ν	$\mathcal{G}_C$ [N/mm]	l [mm]
Metallic	0.7	0	$4.3886e^{-1}$	$6.45e^{-3}$
Ceramic	1.51	0	$7.1158e^{-2}$	$1.9e^{-2}$

Table 1: Materials properties.

5.1 Plate under tension

The first problem under consideration is the classical square plate of unit size (L = 1 mm) given in Figure 7. To point out that, the thickness of the plate, denoted by t, is set equal to 0.0125 mm. This configuration includes a sharp initial sharp notch of length L/2 = 0.5 mm at the centre of the specimen. Regarding the prescribed conditions, a vertical displacement (δ_y) is imposed on the upper side of the plate while the lower side is restrained towards the vertical direction. Regarding the mesh refinement, we employ concentrated discretization scheme around the notch with using 15100 elements.
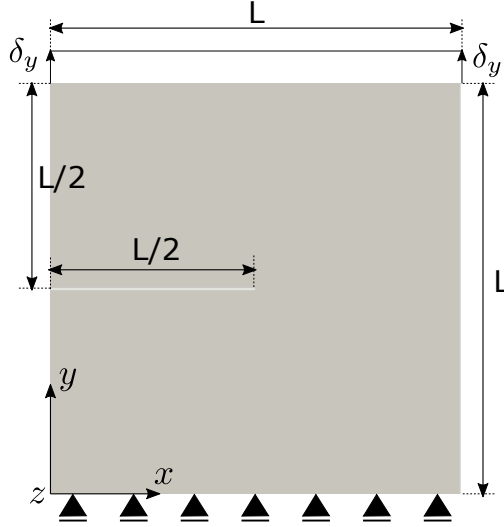

Figure 7: Plate under tension: geometry and boundary conditions.

This problem is simulated for different values of the volume fraction exponent (n) and also for two homogeneous (metallic and ceramic) solid shells. In Figure 8, the stress-strain evolution curves and the contour plot of the phase field variable of the current simulations are given.

Firstly, it can be noticed how depending on the value of the volume fraction exponent (n), the behaviour of the system is changing from fully ceramic ($n=0$) to fully metallic ($n \geq 50$) behaviour. To point out that, the limit cases of the proposed model ($n = 0$ and $n \geq 50$) are established taking into account the variation of the material properties given in Figures 4, 5 and 6. Moreover, in Figure 8, it can be noticed how these limit cases are agreed with the homogeneous solid shell (SS) elements responses.

With reference to the intermediate cases for intermediate values of n, we can see that, as n increases: the dissipated energy, or in other words the area under the stress-strain curve, increases (G_C increases), the stiffness decreases (E decreases) and the maximum stress increases. This is because larger values of n means larger values of the metallic volume fraction (See equations 29, 30 and 31). Therefore, the material properties consistently change with the variation of the constituents in terms of volume fractions via the corresponding gradation law, as depicted in Figures 4, 5 and 6.

The evolution of the maximum stress when n changes is not determined in a straightforward way due to that it is an indirect measure in PF models. However, recalling Equation 6 and knowing that l decreases when n increases, it can be expected bigger values of the maximum stress as n growths.

It is worth mentioning that, in all the cases simulated (homogeneous shells and power-based shells with different values of n) the crack path remains constant and the stress-strain evolution curves present two different stages. The first stage exhibits an increasing stress-strain evolution until a maximum stress is reached. In this stage different events take place: a linear elastic

evolution previous damage initiation, the onset of damage and the stable growth of the crack. However, in the second stage, the unstable growth of the crack happens until the complete failure of the system.

Finally, it is worth to point out that the damage pattern given in Figure 8 replicates that corresponding to the homogeneous case because our material properties in the current formulation are exclusively changing in the thickness direction (ξ^3) instead of in the xy plane. The extension for FGM formulation including both gradation scheme is beyond the matter of the present investigation but of high interest in future activities completing current formulation [47].
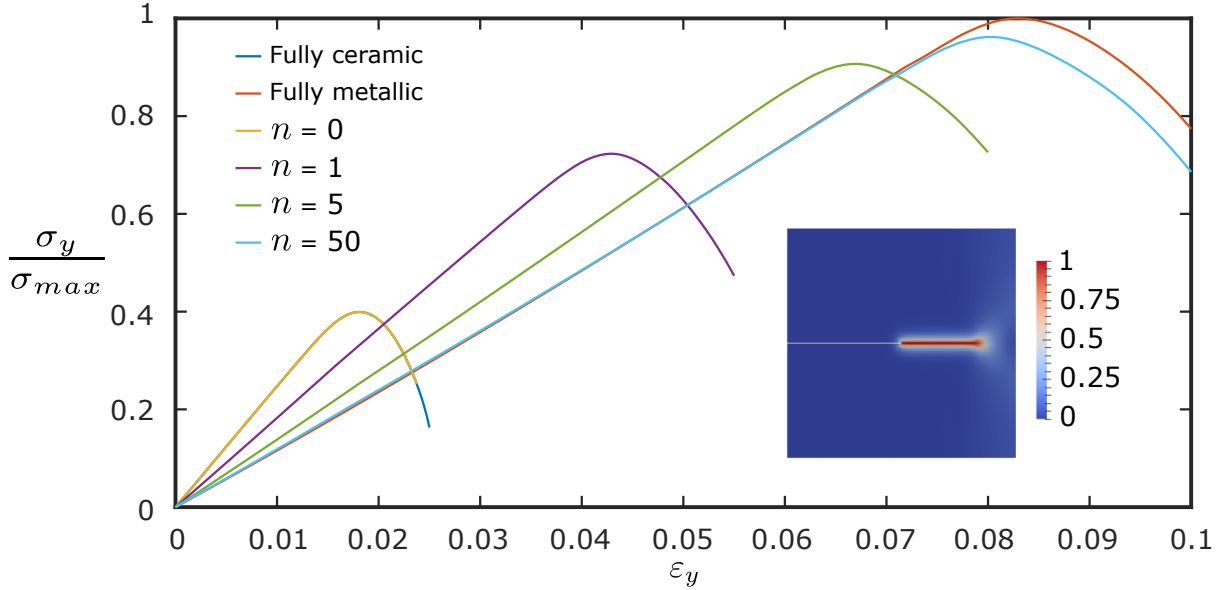

Figure 8: Plate under tension: stress-strain evolution curve and damage pattern (stress of the system/maximum stress, being $\sigma_{max} = 37.45$ N/mm^2.

5.2 Cylindrical shell under tension

In this Section, we aim at assessing the capabilities of the modelling framework in capturing fracture events in curved structures which are here benchmarked. For this purpose, we consider a quarter of a cylindrical shell with an initial sharp notch at the centre of the specimen (See Figure 9). The geometrical parameters are: length L = 340.8 mm, internal radius r_i = 100.1 mm, external radius r_e = 103.1 mm, notch length h = 6 mm and notch width w = 3 mm. Regarding the boundary conditions and complying with the symmetry of the system, the x = 0 side is restrained towards the horizontal direction, while the vertical displacements are restrained at the y = 0. In addition to this, the shell is fully clamped to the z = 0 side, while a uniform displacement (δ_z) is imposed on the z = L side. The geometry is discretized using 9920 elements.

In line with the previous application, the curved shell given in Figure 9 is used to simulate functionally graded power-based shells with different values of the volume fraction exponent (n) and also, two homogeneous (metallic and ceramic) solid shells. The stress-strain evolution curves and the contour plot of the phase field variable of the simulations carried out in the present Section, are given in Figure 10. It can be noticed how the limit cases of the proposed formulation ($n = 0$ and $n \geq 50$) are agreed with the fully ceramic solid shell element and fully metallic solid shell element response, respectively, again pinpointing the robustness of the current methodology. Moreover, for the intermediate cases, the increase of n, which means
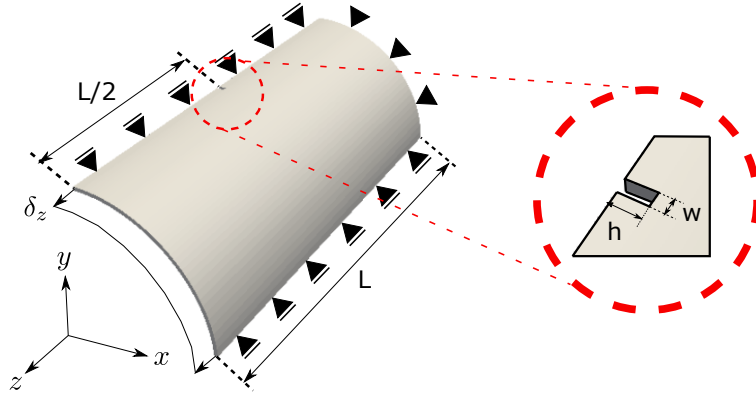
Figure 9: Cylinder under tension: geometry and boundary conditions.

an increase of the metallic constituent, causes the increase of the maximum stress and the dissipated energy (G_C increases). However, this provokes the reduction of the stiffness of our system (E decreases). As in the previous application, the explanation of the maximum stress increase is due to the reduction of l with the growth of n and to the relation given in equation 6.
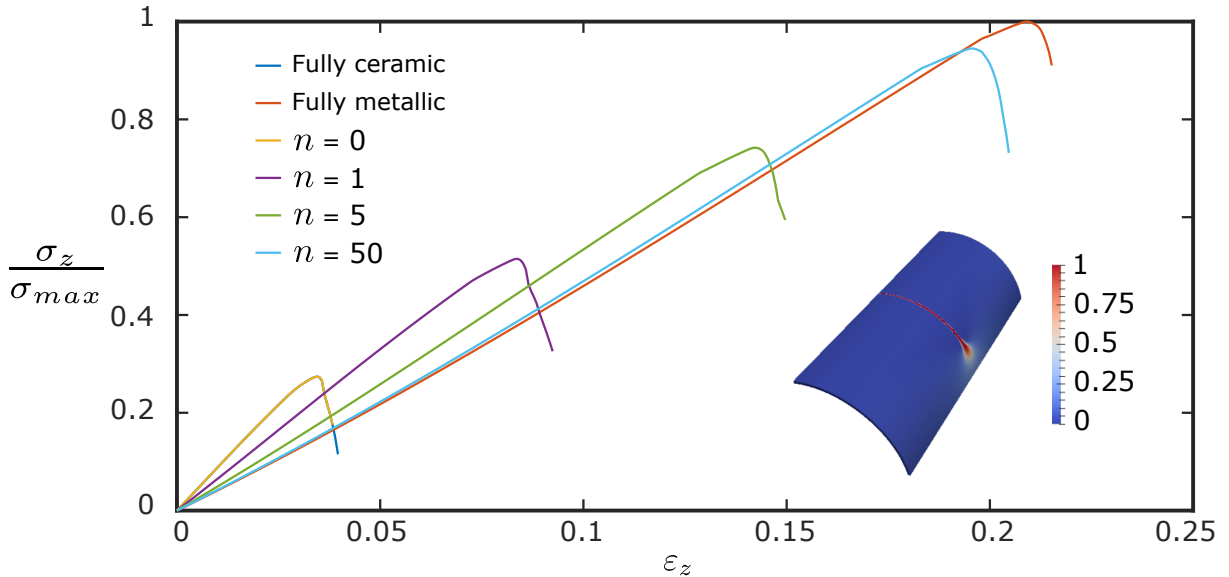

Figure 10: Cylinder under tension: stress-strain evolution curve and damage pattern (stress of the system/maximum stress, being $\sigma_{max} = 171.90$ N/mm^2.

Moreover, to highlight that, the response of the system in all the cases considered (Figure 10) shows the same crack path and two different stages in the stress-strain evolution curve. The first stage shows an increasing stress-strain evolution where 3 different phases are identified: linear elastic evolution before damage, onset of damage and stable growth of the crack. Finally, in the second stage, the stress-strain evolution curve decreases along the loading path due to the unstable growth of the crack.

5.3 Cylindrical shell under tension and bending

Finally, after proving the applicability of the proposed model to the classical square plate and to a curved shell, we benchmark the current apporach for tension-bending problems. To do so, we simulate the cylinder described previous Section, but adding a vertical displacement (δ_y) at
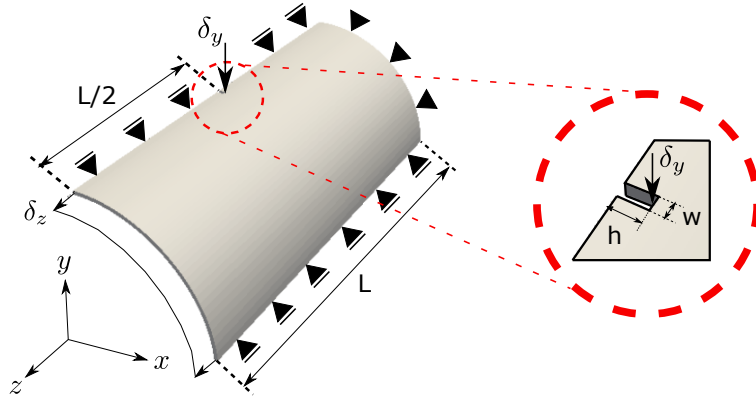
Figure 11: Cylinder under tension and flexion: geometry and boundary conditions.

the top of the notch as we can see in Figure 11.

Again, as in the previous simulations, the results given in Figure 12 show how the response of the system changes from fully ceramic ($n = 0$) to fully metallic ($n \geq 50$) behaviour depending on the value of n. It can be noticed the agreement between the limit cases of the proposed model ($n = 0$ and $n \geq 50$) and the homogeneous solid shell (SS) element responses.

Moreover, as expected, when the volume fraction of the metallic phase increases, in other words when n raises, the maximum stress and the dissipated energy (G_C) increases. However, the stiffness of the system (E) decreases. The explanation of the evolution of the maximum stress with the variation of n is the same as in the previous applications.
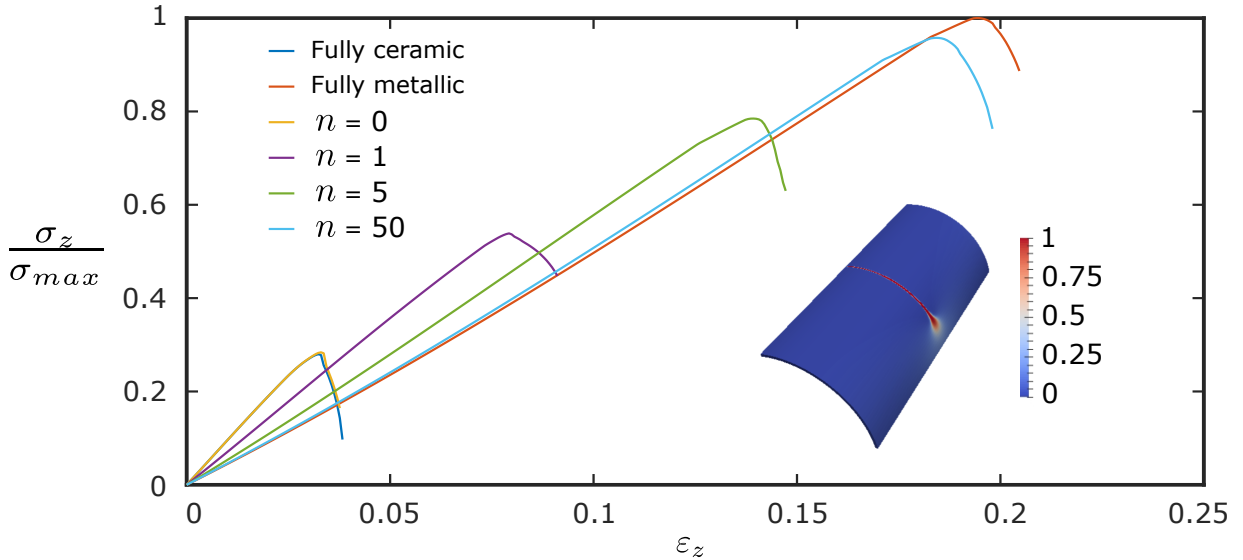

Figure 12: Cylinder under tension and flexion: stress-strain evolution curve and damage pattern (stress of the system/maximum stress, being $\sigma_{max} = 158.86$ N/mm^2).

In Figure 12, again, the different stages of the stress-strain evolution curves detected in the previous simulations are also identifiable: an increasing evolution were three different events happen (linear elastic evolution before damage, onset of damage and stable growth of the crack) and a decreasing evolution due to the unstable crack growth.

To conclude, comparing the results of the cylinder under tension with the current simulations, we can stat that, although the damage pattern and the stiffness of the system is not affected by the inclusion of the vertical displacement δ_y, the maximum stress and the dissipated energy are significantly lower when the vertical displacement δ_y is introduced.

6 Concluding remarks

In the present research, based on the modelling framework of thermodynamic consistent PF approach of fracture, we have presented a novel formulation for triggering fracture events in FG shells. Conversely to former PF methods for shells, the current models is based on a solid shell kinematic model, which was equipped with the EAS and ANS methods in order to obtain a locking-free element formulation. The variational formalism has been constructed using a mixed-formulation that included the regularized Griffith potential due to fracture.

The present model has been formulated for fracture analysis of for FGM shell-based structures. Therefore, this work is pioneering in terms of combining: locking-free shells, FGMs and phase field. In addition, it is remarkable to point out that the proposed model originally allowed the inclusion of the phase field length scale and the fracture toughness as function of the thickness coordinate. The attributes of the model comprised: (i) the efficient fracture initiation and propagation and (ii) the potential use for complex geometries and loading conditions.

Current predictions have shown the applicability of the proposed model to predict fracture in functionally graded power-based shells under in-plane and out-of-plane loading conditions.

Future extensions of the proposed methodology will comprise the incorporation of ductile fracture in conjunction to multi-physic phenomena. From the numerical standpoint, we will pay careful attention on the adoption of a monolithic solution scheme according to the Broyden-Fletcher-Goldfarb-Shanno (BFGS) algorithm (DOI: 10.1016/j.cma.2019.112704).

References

[1] B. Zhu, Y. Cai, A strain rate-dependent enhanced continuum model for elastic-plastic impact response of metal-ceramic functionally graded composites, International Journal of Impact Engineering 133 (2019) 103340.

[2] S. Kumar, K. M. Reddy, A. Kumar, G. R. Devi, Development and characterization of polymer–ceramic continuous fiber reinforced functionally graded composites for aerospace application, Aerospace Science and Technology 26 (1) (2013) 185–191.

[3] J. Jang, S. Han, Mechanical properties of glass-fibre mat/pmma functionally gradient composite, Composites Part A: Applied Science and Manufacturing 30 (9) (1999) 1045–1053.

[4] W. Pompe, H. Worch, M. Epple, W. Friess, M. Gelinsky, P. Greil, U. Hempel, D. Scharnweber, K. Schulte, Functionally graded materials for biomedical applications, Materials Science and Engineering: A 362 (1-2) (2003) 40–60.

[5] D. Mahmoud, M. A. Elbestawi, Lattice structures and functionally graded materials applications in additive manufacturing of orthopedic implants: a review, Journal of Manufacturing and Materials Processing 1 (2) (2017) 13.

[6] R. Vassen, H. Kassner, A. Stuke, D. E. Mack, M. O. D. Jarligo, D. Stöver, Functionally graded thermal barrier coatings with improved reflectivity and high-temperature capability, in: Materials Science Forum, Vol. 631, Trans Tech Publ, 2010, pp. 73–78.

[7] E. Mueller, Č. Drašar, J. Schilz, W. Kaysser, Functionally graded materials for sensor and energy applications, Materials Science and Engineering: A 362 (1-2) (2003) 17–39.

[8] B. Bartczak, D. Gierczycka-Zbrożek, Z. Gronostajski, S. Polak, A. Tobota, The use of thin-walled sections for energy absorbing components: a review, Archives of Civil and Mechanical Engineering 10 (4) (2010) 5–19.

[9] W. Abramowicz, Thin-walled structures as impact energy absorbers, Thin-Walled Structures 41 (2-3) (2003) 91–107.

[10] A. L. Kalamkarov, G. Saha, A. Georgiades, General micromechanical modeling of smart composite shells with application to smart honeycomb sandwich structures, Composite structures 79 (1) (2007) 18–33.

[11] V. Vasiliev, V. Barynin, A. Rasin, Anisogrid lattice structures–survey of development and application, Composite structures 54 (2-3) (2001) 361–370.

[12] E. Wyart, D. Coulon, T. Pardoen, J.-F. Remacle, F. Lani, Application of the substructured finite element/extended finite element method (s-fe/xfe) to the analysis of cracks in aircraft thin walled structures, Engineering Fracture Mechanics 76 (1) (2009) 44–58.

[13] K. Naumenko, V. A. Eremeyev, A layer-wise theory of shallow shells with thin soft core for laminated glass and photovoltaic applications, Composite Structures 178 (2017) 434–446.

[14] P. M. Areias, J. Song, T. Belytschko, Analysis of fracture in thin shells by overlapping paired elements, Computer Methods in Applied Mechanics and Engineering 195 (41-43) (2006) 5343–5360.

[15] X. Zhuang, R. Huang, H. Zhu, H. Askes, K. Mathisen, A new and simple locking-free triangular thick plate element using independent shear degrees of freedom, Finite Elements in Analysis and Design 75 (2013) 1–7.

[16] E. Carrera, M. Cinefra, M. Petrolo, E. Zappino, Finite element analysis of structures through unified formulation, John Wiley & Sons, 2014.

[17] M. B. Dehkordi, S. Khalili, E. Carrera, Non-linear transient dynamic analysis of sandwich plate with composite face-sheets embedded with shape memory alloy wires and flexible core-based on the mixed lw (layer-wise)/esl (equivalent single layer) models, Composites Part B: Engineering 87 (2016) 59–74.

[18] E. Carrera, Theories and finite elements for multilayered plates and shells: a unified compact formulation with numerical assessment and benchmarking, Archives of Computational Methods in Engineering 10 (3) (2003) 215–296.

[19] J. Reinoso, M. Paggi, C. Linder, Phase field modeling of brittle fracture for enhanced assumed strain shells at large deformations: formulation and finite element implementation, Computational Mechanics 59 (6) (2017) 981–1001.

[20] J. Reinoso, G. Catalanotti, A. Blázquez, P. Areias, P. Camanho, F. París, A consistent anisotropic damage model for laminated fiber-reinforced composites using the 3d-version of the puck failure criterion, International Journal of Solids and Structures 126-127 (2017) 37 – 53.

[21] K. Rah, W. Van Paepegem, A.-M. Habraken, J. Degrieck, R. A. de Sousa, R. A. Valente, Optimal low-order fully integrated solid-shell elements, Computational Mechanics 51 (3) (2013) 309–326.

[22] J. Simo, F. Armero, R. Taylor, Improved versions of assumed enhanced strain tri-linear elements for 3d finite deformation problems, Computer methods in applied mechanics and engineering 110 (3-4) (1993) 359–386.

[23] M. Bischoff, E. Ramm, Shear deformable shell elements for large strains and rotations, International Journal for Numerical Methods in Engineering 40 (23) (1997) 4427–4449.

[24] L. Vu-Quoc, X. Tan, Optimal solid shells for non-linear analyses of multilayer composites. i. statics, Computer methods in applied mechanics and engineering 192 (9-10) (2003) 975–1016.

[25] S. Reese, A large deformation solid-shell concept based on reduced integration with hourglass stabilization, International Journal for Numerical Methods in Engineering 69 (8) (2007) 1671–1716.

[26] O. Zienkiewicz, R. Taylor, J. Too, Reduced integration technique in general analysis of plates and shells, International Journal for Numerical Methods in Engineering 3 (2) (1971) 275–290.

[27] J. Reinoso, A. Blázquez, Application and finite element implementation of 7-parameter shell element for geometrically nonlinear analysis of layered cfrp composites, Composite structures 139 (2016) 263–276.

[28] F. Tornabene, E. Viola, Static analysis of functionally graded doubly-curved shells and panels of revolution, Meccanica 48 (4) (2013) 901–930.

[29] E. Carrera, S. Brischetto, M. Cinefra, M. Soave, Effects of thickness stretching in functionally graded plates and shells, Composites Part B: Engineering 42 (2) (2011) 123–133.

[30] J. Reinoso, M. Paggi, P. Areias, A. Blázquez, Surface-based and solid shell formulations of the 7-parameter shell model for layered cfrp and functionally graded power-based composite structures, Mechanics of Advanced Materials and Structures 26 (15) (2019) 1271–1289.

[31] T. Van Do, D. H. Doan, N. D. Duc, T. Q. Bui, Phase-field thermal buckling analysis for cracked functionally graded composite plates considering neutral surface, Composite Structures 182 (2017) 542–548.

[32] R. Arciniega, J. Reddy, Large deformation analysis of functionally graded shells, International Journal of Solids and Structures 44 (6) (2007) 2036–2052.

[33] H. Bayesteh, S. Mohammadi, Xfem fracture analysis of shells: the effect of crack tip enrichments, Computational Materials Science 50 (10) (2011) 2793–2813.

[34] P. M. Areias, T. Belytschko, Non-linear analysis of shells with arbitrary evolving cracks using xfem, International Journal for Numerical Methods in Engineering 62 (3) (2005) 384–415.

[35] P. D. Zavattieri, Modeling of crack propagation in thin-walled structures using a cohesive model for shell elements, Journal of applied mechanics 73 (6) (2006) 948–958.

[36] I. Scheider, W. Brocks, Cohesive elements for thin-walled structures, Computational Materials Science 37 (1-2) (2006) 101–109.

[37] C. G. Dávila, P. M. P. R. d. Camanho, A. Turon Travesa, et al., Cohesive elements for shells, © NASA TP Technical Reports, 2007, núm. 214869.

[38] M. Paggi, P. Wriggers, Stiffness and strength of hierarchical polycrystalline materials with imperfect interfaces, Journal of the Mechanics and Physics of Solids 60 (4) (2012) 557–572.

[39] J. Reinoso, M. Paggi, A consistent interface element formulation for geometrical and material nonlinearities, Computational Mechanics 54 (6) (2014) 1569–1581.

[40] B. Bourdin, G. A. Francfort, J.-J. Marigo, Numerical experiments in revisited brittle fracture, Journal of the Mechanics and Physics of Solids 48 (4) (2000) 797–826.

[41] T.-T. Nguyen, J. Yvonnet, M. Bornert, C. Chateau, K. Sab, R. Romani, R. Le Roy, On the choice of parameters in the phase field method for simulating crack initiation with experimental validation, International Journal of Fracture 197 (2) (2016) 213–226.

[42] E. Tanné, T. Li, B. Bourdin, J.-J. Marigo, C. Maurini, Crack nucleation in variational phase-field models of brittle fracture, Journal of the Mechanics and Physics of Solids 110 (2018) 80 – 99.

[43] C. Miehe, F. Welschinger, M. Hofacker, Thermodynamically consistent phase-field models of fracture: Variational principles and multi-field fe implementations, International Journal for Numerical Methods in Engineering 83 (10) (2010) 1273–1311.

[44] T. K. Mandal, V. P. Nguyen, J.-Y. Wu, Length scale and mesh bias sensitivity of phase-field models for brittle and cohesive fracture, Engineering Fracture Mechanics 217 (2019) 106532.

[45] J.-Y. Wu, Robust numerical implementation of non-standard phase-field damage models for failure in solids, Computer Methods in Applied Mechanics and Engineering 340 (2018) 767–797.

[46] A. Quintanas-Corominas, J. Reinoso, E. Casoni, A. Turon, J. Mayugo, A phase field approach to simulate intralaminar and translaminar fracture in long fiber composite materials, Composite Structures 220 (2019) 899–911.

[47] E. Martínez-Pañeda, A. Golahmar, C. F. Niordson, A phase field formulation for hydrogen assisted cracking, Computer Methods in Applied Mechanics and Engineering 342 (2018) 742–761.

[48] M. Paggi, J. Reinoso, Revisiting the problem of a crack impinging on an interface:a modeling framework for the interaction between the phase field approach for brittle fracture and the interface cohesive zone model, Computer Methods in Applied Mechanics and Engineering 321 (2017) 145 – 172.

[49] T. T. Nguyen, J. Yvonnet, Q. Z. Zhu, M. Bornert, C. Chateau, A phase field method to simulate crack nucleation and propagation in strongly heterogeneous materials from direct imaging of their microstructure, Engineering Fracture Mechanics 139 (2015) 18–39.

[50] V. Carollo, J. Reinoso, M. Paggi, A 3d finite strain model for intralayer and interlayer crack simulation coupling the phase field approach and cohesive zone model, Composite Structures 182 (2017) 636 – 651.

[51] M. Ambati, T. Gerasimov, L. De Lorenzis, Phase-field modeling of ductile fracture, Computational Mechanics 55 (5) (2015) 1017–1040.

[52] S. Natarajan, R. K. Annabattula, E. Martínez-Pañeda, et al., Phase field modelling of crack propagation in functionally graded materials, Composites Part B: Engineering 169 (2019) 239–248.

[53] F. Amiri, D. Millán, Y. Shen, T. Rabczuk, M. Arroyo, Phase-field modeling of fracture in linear thin shells, Theoretical and Applied Fracture Mechanics 69 (2014) 102–109.

[54] J. Kiendl, M. Ambati, L. De Lorenzis, H. Gomez, A. Reali, Phase-field description of brittle fracture in plates and shells, Computer Methods in Applied Mechanics and Engineering 312 (2016) 374–394.

[55] J. Reinoso, A. Arteiro, M. Paggi, P. Camanho, Strength prediction of notched thin ply laminates using finite fracture mechanics and the phase field approach, Composites Science and Technology 150 (2017) 205 – 216.

[56] J. Reinoso, A. Blázquez, Geometrically nonlinear analysis of functionally graded power-based and carbon nanotubes reinforced composites using a fully integrated solid shell element, Composite Structures 152 (2016) 277–294.

[57] R. L. Taylor, FEAP - finite element analysis program (2014).
URL http://www.ce.berkeley/feap